

See discussions, stats, and author profiles for this publication at: <https://www.researchgate.net/publication/256663854>

3D Branched Nanowire Photoelectrochemical Electrodes for Efficient Solar Water Splitting

ARTICLE in ACS NANO · SEPTEMBER 2013

Impact Factor: 12.88 · DOI: 10.1021/nn404170y · Source: PubMed

CITATIONS

45

READS

120

8 AUTHORS, INCLUDING:



Alireza Kargar

University of California, San Diego

46 PUBLICATIONS 349 CITATIONS

SEE PROFILE



Yi Jing

University of California, San Diego

16 PUBLICATIONS 460 CITATIONS

SEE PROFILE



Gun-Young Jung

Gwangju Institute of Science and Technology

115 PUBLICATIONS 2,667 CITATIONS

SEE PROFILE



Deli Wang

University of California, San Diego

75 PUBLICATIONS 7,688 CITATIONS

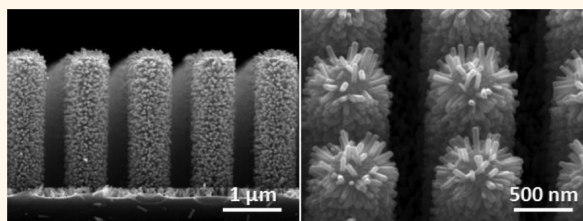
SEE PROFILE

3D Branched Nanowire Photoelectrochemical Electrodes for Efficient Solar Water Splitting

Alireza Kargar,[†] Ke Sun,[†] Yi Jing,[†] Chulmin Choi,[‡] Huisu Jeong,[§] Gun Young Jung,[§] Sungho Jin,[‡] and Deli Wang^{*,†,‡,||}

[†]Department of Electrical and Computer Engineering, [‡]Materials Science and Engineering Program, and ^{||}Qualcomm Institute, University of California—San Diego, 9500 Gilman Drive, La Jolla, California 92093, United States and [§]School of Materials Science and Engineering, Gwangju Institute of Science and Technology (GIST), 123 Cheomdan-gwagiro (Oryong-dong), Buk-gu, Gwangju 500-712, Republic of Korea

ABSTRACT We report the systematic study of 3D ZnO/Si branched nanowire (b-NW) photoelectrodes and their application in solar water splitting. We focus our study on the correlation between the electrode design and structures (including Si NW doping, dimension of the trunk Si and branch ZnO NWs, and b-NW pitch size) and their photoelectrochemical (PEC) performances (efficiency and stability) under neutral conditions. Specifically, we show that for b-NW electrodes with lightly doped p-Si NW



core, larger ZnO NW branches and longer Si NW cores give a higher *photocathodic* current, while for b-NWs with heavily doped p-Si NW trunks smaller ZnO NWs and shorter Si NWs provide a higher *photoanodic* current. Interestingly, the photocurrent turn-on potential decreases with longer p-Si NW trunks and larger ZnO NW branches resulting in a significant photocathodic turn-on potential shift of ~ 600 mV for the optimized ZnO/p-Si b-NWs compared to that of the bare p-Si NWs. A photocathode energy conversion efficiency of greater than 2% at -1 V versus Pt counter electrode and in neutral solution is achieved for the optimized ZnO/p-Si b-NW electrodes. The PEC performances or incident photon-to-current efficiency are further improved using Si NW cores with smaller pitch size. The photoelectrode stability is dramatically improved by coating a thin TiO_2 protection layer using atomic-layer deposition method. These results provide very useful guidelines in designing photoelectrodes for selective solar water oxidation/reduction and overall spontaneous solar fuel generation using low cost earth-abundant materials for practical clean solar fuel production.

KEYWORDS: branched nanowire (b-NW) heterostructures · photoelectrochemical (PEC) cells · water splitting · oxidation · reduction

Branched nanowires (b-NWs)^{1–5} have recently attracted considerable attention for solar energy conversion^{6–20} and energy storage devices^{13,20–23} because of their unique properties such as nanoscale integration of different functional materials, greatly enhanced junction, and surface area, *etc.* b-NWs can be either homojunctions^{6,7,9,10,12,13,15,18,19,21} or heterostructures^{1,2,8,11,17,22} using facile and scalable fabrication methods such as hydrothermal^{7,11,17–19} or solvothermal growth methods⁶ and VLS-CVD gas-phase synthesis methods.^{1,2} Homo b-NWs have been used as anodes in lithium-ion batteries (LIBs),^{13,21} photoanodes in dye-sensitized solar cells (DSSCs),^{6,9,12,15,16,18,19} and photoelectrochemical (PEC) solar cells,^{7,10} *etc.* Hetero b-NWs made of two different materials have also been shown to have different device

applications such as LIB anodes,²² pseudocapacitive energy storage devices,²³ photocatalysts,⁸ and PEC cathodes.¹¹ The larger surface area of b-NWs compared to that of NWs results in higher capacity in LIBs.^{21,22} ZnO^{6,9,12,18} or TiO_2 ¹⁹ b-NWs provide better photovoltaic performance in DSSCs compared to straight ZnO or TiO_2 NWs due to their higher dye loading/absorption and increased light absorption. The efficient charge separation in flower-like CuO/ZnO NWs also showed enhanced photocatalytic activity.⁸

For PEC solar hydrogen production, b-NW arrays are also better candidates compared to single composition NWs or core/shell NW (cs-NW) heterostructures because of their improved reaction surface area, increased light absorption,^{11,24} and enhanced gas evolution efficiency.¹¹ The NW branches

* Address correspondence to deliwang@eng.ucsd.edu.

Received for review August 9, 2013 and accepted September 9, 2013.

Published online September 09, 2013
10.1021/nn404170y

© 2013 American Chemical Society

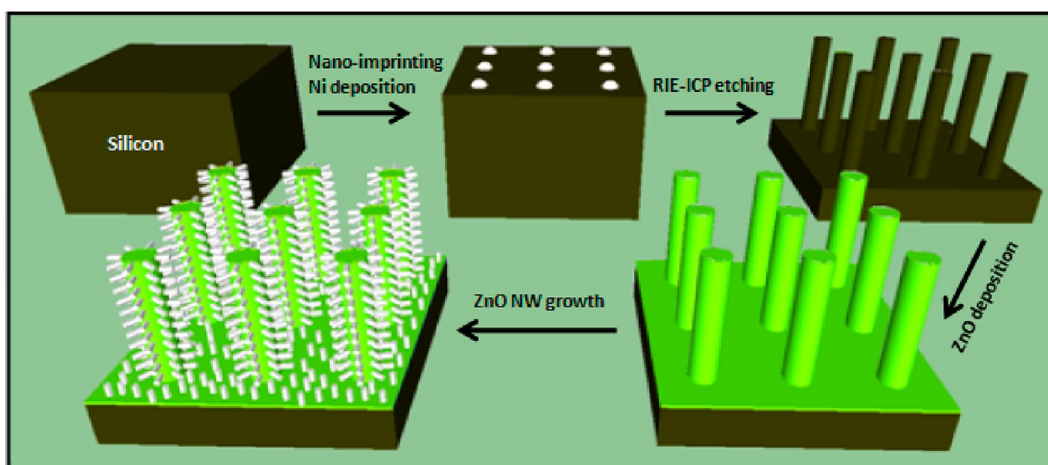


Figure 1. Fabrication procedure for 3D ZnO/Si branched NW (b-NW) arrays. After Si etching, the Ni disks at the head of Si NWs were removed by the Ni etchant.

normally have much smaller sizes compared to NW cores, which can also lead to more efficient charge separation and collection due to close proximity between the photogenerated carriers and the semiconductor-electrolyte interface.⁷ Moreover, b-NW heterostructures, synthesized with two different materials with small and large band gaps, provide broadband absorption and enhanced charge separation compared to the NWs or homo b-NWs. For example, ZnO/Si b-NW heterostructures show very efficient photocathodic hydrogen production.¹¹ More interestingly, selective oxidation or reduction of water using b-NW photoelectrodes are demonstrated by simple changing of the NW core doping concentration,²⁵ which is a very interesting feature paving the way for accomplishing solar fuel cells to perform overall solar water splitting without external bias for practical hydrogen production.^{26,27}

In this paper, we present the systematic study of 3D ZnO/Si b-NW electrodes to improve their photocathodic and anodic performances, and b-NW photoelectrode stability improvement. The PEC performances are optimized in neutral medium based on different dimensions and doping concentrations of NWs as well as the NW array pitch size. The b-NW photoelectrode conversion and incident photon-to-current efficiencies are also studied. Finally, the b-NW electrode stability is investigated in detail with/without protection layer.

RESULTS AND DISCUSSION

The Si NW cores were first fabricated using dry etching, and ZnO NW branches were then grown using the hydrothermal growth method (see Figure 1 for the fabrication procedure and the Methods for details). For convenience, ZnO/Si b-NW arrays for different ZnO NW growth and Si NW etching times are denoted as “b(Xm-ZnO/Ym-p-Si) NWs” and “b(Xm-ZnO/Ym-p⁺-Si) NWs” for NWs with p-Si and p⁺-Si NW cores, respectively. “X” and “Y” are the ZnO growth and Si etching times in

min (m), respectively (for example, “5m-ZnO” means ZnO NWs grown for 5 min or “10m-p-Si” means p-Si NWs etched for 10 min). Figure 2 shows the scanning electron microscopy (SEM) images of 3D ZnO/Si b-NWs with 10m-Si NW cores and ZnO NW branches grown for different times (bare Si NW array is considered as zero ZnO growth time (Figure 2a–c)). The average Si etching rate is $\sim 0.24 \mu\text{m}/\text{min}$, the Si NW array pitch size is $\sim 1 \mu\text{m}$, and the Si NW diameters are $\sim 280 \text{ nm}$ and $\sim 230 \text{ nm}$ for 10 and 20 min etchings, respectively (see Figure S1, Supporting Information). Note that we used the same nanoimprinted Si substrates to make all the Si NW samples; however, the Si NW diameters after RIE-ICP etching are smaller than the dot size of the nanoimprinting mold (which was 500 nm), and the longer etching time results in a smaller diameter. In the applied RIE-ICP etching process, the C_4F_8 gas forms a passivation layer on the NW sidewall while the SF_6 etch gas etches this passivation layer and Si.²⁸ If the C_4F_8 flow is not high enough, the passivation layer is not thick enough to protect the NW sidewall. Therefore, the Si NW becomes thinner with increasing the etching time. Note that we fixed the C_4F_8 flow for all samples with the aim of identical etching conditions. As shown in Figure 2d–i, there is a uniform growth of ZnO NW branches in length on Si NW cores, and ZnO NWs cover the entire length of Si NW trunks as well as on flat surface between Si NWs. Longer ZnO growth time leads to bigger ZnO NW branches (larger diameter and longer length). The average ZnO NW lengths (on 10m-Si NW backbones) are ~ 90 and $\sim 200 \text{ nm}$ for 5 and 10 min ZnO growth times, respectively. The 10m-ZnO NWs have higher density than 5m-ZnO NWs, which can be due to longer ZnO growth time. Low-magnification SEM images in Figure 2j–l indicate uniform formation of b-NWs over a large area, indicating the scalability of our processing for large area photoelectrodes from the low cost materials.

Figure 3 exhibits SEM images of 10m-ZnO NW branches on Si NW cores etched for two different times

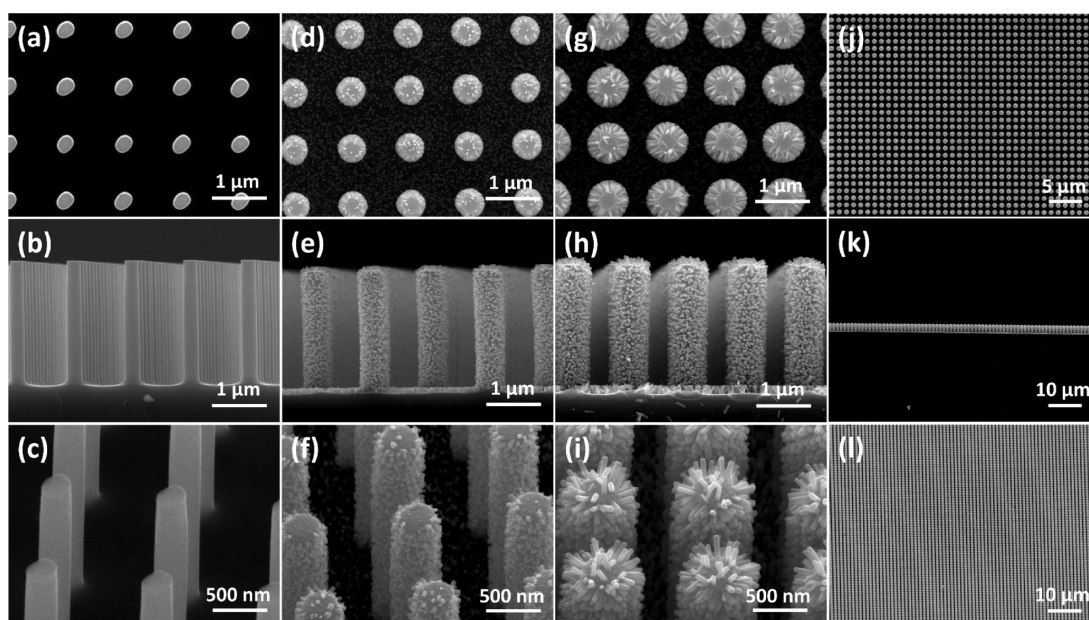


Figure 2. SEM images of 3D ZnO/Si b-NWs of 10m-Si NW cores with different ZnO NW growth times. First row, second row, and third row show the top view, cross-sectional view, and 45° view images, respectively. (a–c) zero min (bare Si NW array), (d–f) 5 min, and (g–i) 10 min. (j–l) Low-magnification images of (g–i).

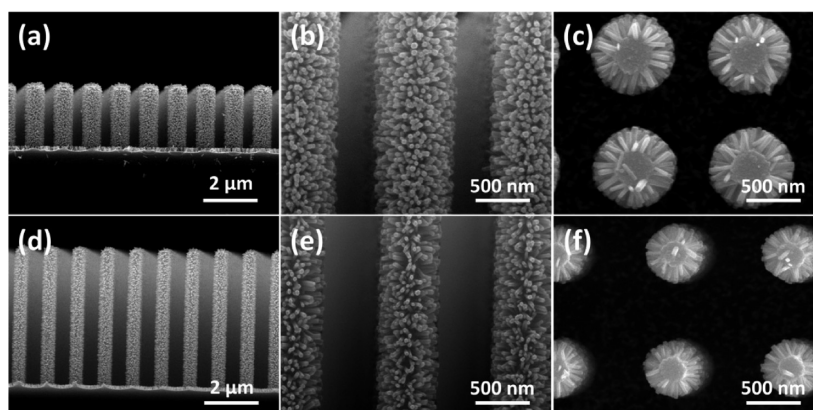


Figure 3. SEM images of 3D ZnO/Si b-NWs with 10m-ZnO NW branches on Si NW cores with (a–c) 10 min and (d–f) 20 min RIE etching. First and second columns show the cross-sectional view images, and third column shows the top view images.

(10 min, top row, and 20 min, bottom row). Smaller ZnO NWs were found on longer Si NW cores (shorter length and smaller diameter) (Figure 3e,f *versus* Figure 3b,c) for the same ZnO growth time of 10 min due to reaction limited ZnO NW growth. The average ZnO NW lengths are ~ 200 nm and ~ 140 nm for 10 and 20 min etching times, respectively. Note that even for long Si NWs (Figure 3d), the ZnO NWs also cover the entire length of Si NW backbones and the flat surface between the Si NWs.

The effect of ZnO NW growth time, and consequently NW branch diameters, on the photocurrent of ZnO/p-Si b-NWs is illustrated in Figure 4a. Compared to the minimal photocathodic current from the bare Si NW electrodes (inset of Figure 4a), the b-NWs provide much enhanced photocathodic current due to their improved charge separation coming from p-Si

and n-ZnO NWs junction, increased reaction surface area, enhanced light absorption, and improved gas evolution.²⁵ Larger ZnO NW branches give higher photocathodic current because of the increased surface area. Figure 4b illustrates the transient current density under chopped light illumination for corresponding samples at -1.5 V external bias. The dark current densities of corresponding samples are shown in Figure 4c. The higher photocurrents and dark currents from b-NW electrodes with larger ZnO NW branches under chopped light illumination (Figure 4b) are similar to those in Figure 4a,c. Figure 4d,e shows the effect of Si NW length on the photocathodic current under constant and chopped light illumination. Longer Si NW (20m-p-Si NW) cores lead to higher photocathodic currents mainly due to enhanced light absorption²⁹ and increased total surface area of b-NWs. Note that

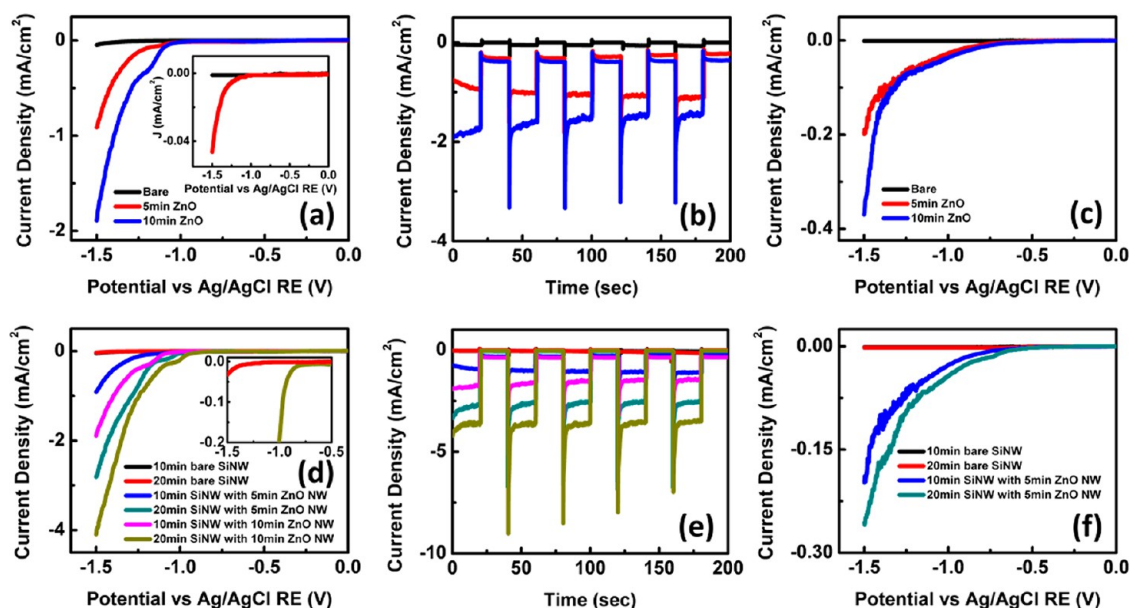


Figure 4. (a) Photocurrent density of 10m-p-Si NW cores with ZnO NW branches grown for different times, (b) transient current density under chopped light illumination of corresponding b-NW samples at -1.5 V, and (c) dark current density of corresponding samples in (a). The inset in (a) shows the dark (black curve) and photo (red curve) currents of bare 10m-p-Si NW array. (d) Photocurrent density of p-Si NW trunks etched for different times with ZnO NW branches grown for various times, (e) transient current density of corresponding samples at -1.5 V, and (f) dark current density of various etched p-Si NW cores with different ZnO NW branches (corresponding samples in (d)). The inset in (d) shows the zoom-in photocurrents of bare 20m-Si NW array and b(10m-ZnO/20m-p-Si) NWs.

20 min RIE also leads to a smaller diameter (Figure 3 and Figure S1, Supporting Information) and potentially better charge separation and consequently higher photocurrent due to larger band bending at the junction between p-Si and n-ZnO NWs.²⁵ Also note that even for the same ZnO growth time, the ZnO NW branches are smaller and denser for longer p-Si NW cores (Figure 3), leading to more efficient charge separation and collection, as well as further increase in the overall surface area. At forward biasing conditions, there is a much smaller photoanodic current, compared to the photocathodic current (data not shown), particularly for b-NWs with longer p-Si NW cores. The increased dark current for b-NWs with longer cores (Figure 4f) confirms the enhanced surface area. The photocathodic current overshoot when switching on light (Figure 4e) can be from the accumulation of photogenerated electrons at the NWs-electrolyte interface, which subsequently recombine with holes at the interface until a stationary photocurrent is reached.

Very interestingly, the photocurrent turn-on potential reduces (the photocathodic turn-on potential shifts toward more positive potentials) with longer Si NW cores and larger ZnO NW branches. Note that there is a significant shift of ~ 600 mV toward positive voltages for b(10m-ZnO/20m-p-Si) NWs compared to 20m-p-Si NW array, which was determined with reference to the photocurrent of bare 20m-Si NW array at -1.5 V (inset of Figure 4d). The photocathodic turn-on potential of b(10m-ZnO/20m-p-Si) NWs is about -0.3 V versus reversible hydrogen electrode (RHE) (Figure S2,

Supporting Information). The transient current density under chopped illumination and at -1.5 V for corresponding samples is shown in Figure 4e confirming the observed trends in Figure 4d. The photocathode energy conversion efficiency for hydrogen evolution of the optimized ZnO/p-Si b-NWs is over 2% at the biasing potential of -1 V versus Pt counter electrode (CE) using two-electrode PEC measurement setup and considering no optical losses coming from the PEC setup (see Figure S3a, Supporting Information, and its inset for the plots of photocurrent density and efficiency versus applied potential in two-electrode setup, and the Supporting Information for the conversion efficiency calculation). The three-electrode measurement setup provides a photocathode efficiency of over 3.5% at -1.26 V versus normal hydrogen electrode (NHE), revealing the efficiency overestimation using three-electrode setup (see Figure S3b, Supporting Information, and inset and the Supporting Information for more details). Longer Si and ZnO NWs than those investigated here can also further improve the PEC performances.

The effect of Si NW array pitch size (b-NW center-to-center spacing) (see Figure S4, Supporting Information, and the Supporting Information for the investigated dimensions) on the photocathodic performance of ZnO/p-Si b-NWs is studied and is found to play a significant role in increasing the photocathode conversion efficiency (Figure S5, Supporting Information). The smaller pitch size, with smaller core diameter, offers much higher photocathodic current and also shifts the photocathodic turn-on potential toward

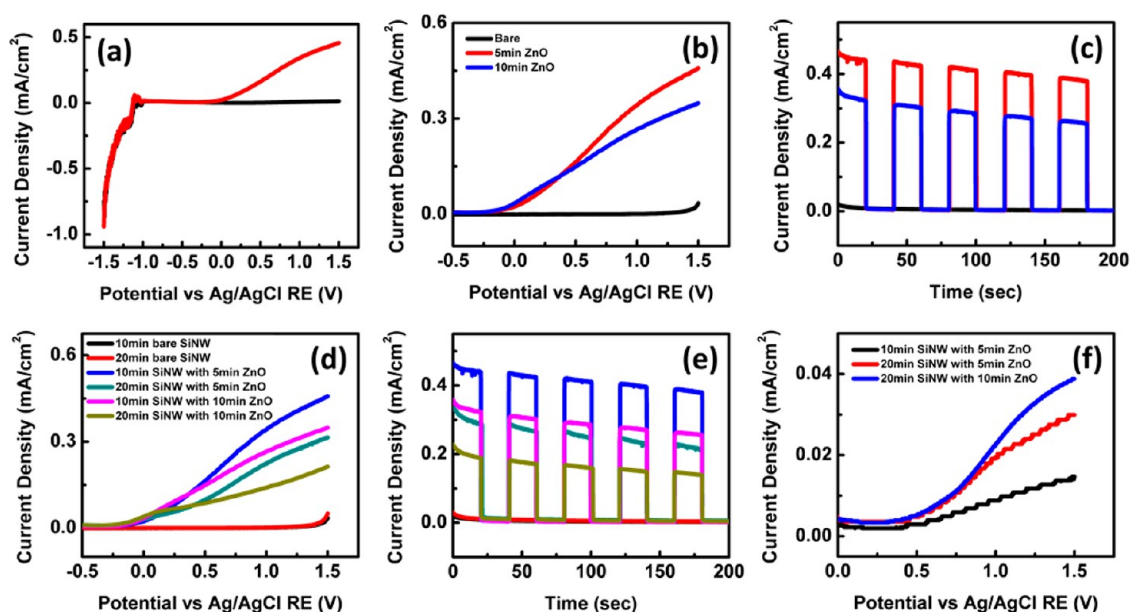


Figure 5. (a) Current density of b(5m-ZnO/10m- p^+ -Si) NWs. The red and black lines represent the photocurrent and dark current densities, respectively. (b) Photocurrent density of 10m- p^+ -Si NW cores with ZnO NW branches grown for various times, and (c) transient current density under chopped light illumination of corresponding b-NWs at +1.5 V. (d) Photocurrent density of p^+ -Si NW backbones etched for different times with different ZnO NW branches. (e) Transient current density of corresponding samples at +1.5 V. (f) Dark current density of various p^+ -Si NW cores with different ZnO NW branches (corresponding samples in (d)).

more positive potentials, which is probably due to enhanced light absorption and increased total surface reaction area of b-NWs (see the Supporting Information for more details).

We have recently demonstrated the photoanodic behavior using ZnO/ p^+ -Si b-NWs, namely tuning of PEC electrode functions by changing the Si NW core doping.²⁵ In fact, under reversed biasing condition, there is no difference between dark and photo currents meaning that there is no photocathodic behavior (see Figure 5a as an example). Note that all the tested b-NW samples with p^+ -Si NW cores did not show any photocathodic current, indicating that this behavior is universal, regardless of p^+ -Si or ZnO NW dimensions. Note also that our focus in this study is to optimize this photoanodic behavior of ZnO/ p^+ -Si b-NWs for more efficient water oxidation. Figure 5b illustrates the effect of ZnO growth time on the photoanodic behavior. The ZnO/ p^+ -Si b-NWs exhibit a large photoanodic current compared to the bare NW array, which does not show any photoanodic behavior (Figure 5c). The photoanodic current increases with reducing ZnO growth time due to lower recombination for photogenerated carriers. This is easily understandable as, for b-NWs with shorter ZnO NW branches, the photogenerated electrons at the ZnO-electrolyte interface have shorter travel distance to the p^+ -Si region, resulting in lower recombination with holes at the interface and consequently larger photoanodic current and more water oxidation.²⁵ The transient current density under chopped illumination for corresponding b-NWs at +1.5 V (Figure 5c) confirms the trend in Figure 5b.

The effect of p^+ -Si NW core length is shown in Figure 5d, in which the photoanodic current decreases with increasing length probably due to longer transport pathway for photogenerated carriers resulting in increased recombination. The dark current, on the other hand, shows the opposite trend because of its improved surface area (Figure 5f). Note that the stepwise shape of the current curves in Figure 5f is because dark currents are very low, and the sensitivity was selected to be the same for the current scan of all samples. Because of the small minority carrier diffusion length and short minority carrier lifetime of p^+ -Si NW trunks, they cannot produce a considerable amount of carriers,²⁵ thus, higher absorption of longer p^+ -Si NW cores is not effective in the improved photocurrent. Note that the photoanodic current of b-NWs with 20m- p^+ -Si NWs shows the same trend for different ZnO growth times as that for b-NWs with 10m- p^+ -Si NWs, while the dark current increases with increasing ZnO growth time (see Figure 5f) because of the increased surface area. The transient current density (Figure 5e) confirms the observed trends in Figure 5d.

The observed trends for the photoanodic current of ZnO/ p^+ -Si b-NWs are different from those for the photocathodic current of ZnO/ p -Si b-NWs because the p -Si NW cores contribute to improving the photocathodic current because of the effective junction between p -Si and n -ZnO NWs leading to enhanced charge separation, while the junction between p^+ -Si and n -ZnO NWs is not effective for charge separation.²⁵ The anodic turn-on potential does not significantly change with altering Si NW etching or ZnO growth

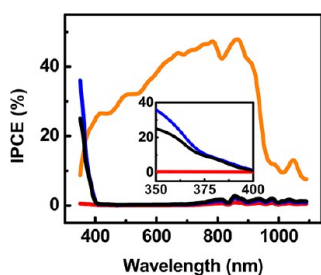


Figure 6. IPCE for the b(5m-ZnO/10m-p-Si) NWs at -1.3 V (orange line) and the 10m-p $^{+}$ -Si NW cores with various ZnO NW branches at $+1.3$ V (red: bare Si NW array, blue: 5 min ZnO, black: 10 min ZnO). The inset shows the zoom-in spectral IPCE in UV range for the corresponding samples with p $^{+}$ -Si NW cores. These b-NW arrays were coated with a 20 nm TiO $_2$ layer.

time (Figure 5d), while as observed in Figure 4d, there is a shift in cathodic turn-on potential with these changes for the ZnO/p-Si b-NWs. This may be explained by the fact that in ZnO/p-Si b-NW heterostructures the effective Si–ZnO junction delivers photogenerated carriers toward the ZnO–liquid junction for surface reactions and the higher surface area of longer Si NWs or larger ZnO NWs, providing higher surface reactions can further shift the turn-on potential. But for the ZnO/p $^{+}$ -Si b-NWs, as mentioned above, the Si–ZnO junction is not effective and the photogenerated carriers are mainly produced by the ZnO–liquid junction, in which shorter Si NWs or smaller ZnO NWs experience less recombination. Moreover, unlike the ZnO/p-Si b-NWs, there is no current overshoot for different p $^{+}$ -Si NW etching or ZnO growth times in the ZnO/p $^{+}$ -Si b-NWs.

The PEC performance of the b-NWs is further evaluated using spectral IPCE (see the Methods). The studied samples for the IPCE (except bare Si NW samples) were coated with a 20 nm TiO $_2$ using atomic layer deposition (ALD) to improve the stability of samples and to have stationary current during the IPCE measurement. The spectral IPCE for b(5m-ZnO/10m-p-Si) NWs at -1.3 V (orange line) is shown in Figure 6, exhibiting a broadband photoresponse due to combination of p-Si and ZnO NWs. Note that the IPCE for this sample was measured after long stability test, in which there was a constant photocurrent. The small peak at ~ 1050 nm is due to Si material though the reason for that is not entirely clear at this point. The ZnO/p-Si b-NWs show much higher IPCE than the bare p-Si NW array (data not shown here), which can be due to effective Si–ZnO junction, increased surface area, and probably improved light absorption.^{11,24} The photoanodic behavior of the ZnO/p $^{+}$ -Si b-NWs has been confirmed with their spectral photoresponse which lies below 400 nm due to ZnO band gap.²⁵ The IPCE for 10m-p $^{+}$ -Si NW cores with different ZnO NW branches at $+1.3$ V is illustrated in Figure 6, exhibiting the same trend as that for the photoanodic current (Figure 5b).

Higher IPCE for smaller ZnO NW can be due to the reduced recombination discussed above. The photoresponse lies below 400 nm for different ZnO growth times and there is no photoresponse for the bare p $^{+}$ -Si NW array. The effect of p-Si and p $^{+}$ -Si NW core lengths was also investigated (data not shown here) exhibiting the same trends as those in the J - V measurements.

Long-term stability, besides hydrogen production cost and efficiency, is another key factor for practical industrial hydrogen production. Due to material instability, ZnO/Si b-NW photoelectrodes cannot offer long-term stability. Using a corrosion-resistant TiO $_2$ coating layer and with and without Pt cocatalyst, b-NW electrodes' stabilities over a long time were investigated. Figure 7a,b shows the SEM images of b(5m-ZnO/10m-p-Si) NWs covered with 20 nm TiO $_2$ layer and 3 nm Pt cocatalyst. The TiO $_2$ layer covers the surfaces of the NWs and substrate over the entire sample (see Figure S6, Supporting Information). Also note that the Pt nanoparticles are hard to recognize from the SEM images due to their very small thickness. The current density of b(5m-ZnO/10m-p-Si) NWs with different coatings is shown in Figure 7c. The dark current and photocurrents of TiO $_2$ -coated b-NW electrode reduce compared to that of the bare b-NW one, and the photocurrent reduction is mainly at high reversed biasing potentials (see Figure 7c inset). On the other hand, the dark current and photocurrents of TiO $_2$ /Pt-coated b-NW electrodes increase compared to that of the bare b-NWs; in particular, the photocurrent improves significantly. More importantly, the Pt cocatalyst shifts the photocathodic current turn-on potential toward positive potentials for ~ 480 mV. Note that we expect a similar potential shift for the Pt-coated b-NWs (without any TiO $_2$ coating) due to the negligible photocathodic current reduction of the TiO $_2$ -coated b-NWs at low reversed biasing potentials (Figure 7c inset). The turn-on potential shift for the optimized bare b(10m-ZnO/20m-p-Si) NWs is ~ 260 mV compared to the turn-on potential of bare b(5m-ZnO/10m-p-Si) NWs, which is over half of what is achieved by Pt cocatalyst on the TiO $_2$ -coated b-NWs (~ 480 mV). This is another interesting feature of these b-NW photoelectrodes showing that significant turn-on potential shift can be obtained even without using costly Pt cocatalyst through optimizing the b-NWs. By further optimization (smaller Si NW pitch size, longer Si NWs, or larger ZnO NWs), it may be possible to achieve similar turn-on potential shift to that of TiO $_2$ /Pt coated sample. The switching behavior of TiO $_2$ /Pt coated b-NWs is investigated using the current density under chopped light illumination (Figure 7d), in which the sample exhibits good switching behavior without any current overshoot. The transient current density under pulsed illumination also showed the same good switching behavior without current overshoot demonstrating

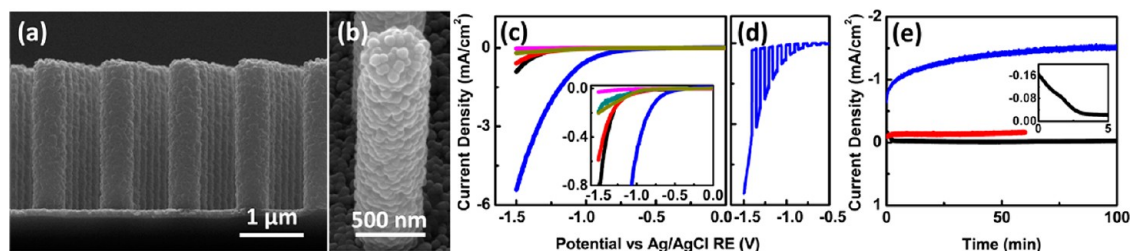


Figure 7. (a–b) SEM images of TiO_2/Pt -coated b(5m-ZnO/10m-p-Si) NWs. (c) Current density of b(5m-ZnO/10m-Si) NWs with different coatings (dark cyan and black lines: dark and photo currents of bare b-NWs, respectively, magenta and red lines: dark and photo currents of TiO_2 -coated b-NWs, respectively, dark yellow and blue lines: dark and photo currents of TiO_2/Pt coated b-NWs, respectively). The inset shows the corresponding zoomed-in curves. (d) Current density of TiO_2/Pt coated b-NWs under chopped illumination. (e) Current density under illumination *versus* time of corresponding samples in (c) (black line: bare, red line: TiO_2 -coated, and blue line: TiO_2/Pt coated). The inset exhibits the enlarged first part (0–5 min) of curve for bare b-NWs. The applied external potential is -1 V for all curves in (e).

that charge carriers accumulation at the electrode surface is not that significant in these samples like that observed for the bare b-NWs (Figure 4).

Photocurrent stability tests for b(5m-ZnO/10m-p-Si) NWs with different coatings were carried out by collecting their currents under a fixed illumination of 100 mW/cm^2 and at a biasing potential of -1 V (Figure 7e). The photocurrent for bare b-NW sample decreases significantly after a few minutes (inset of Figure 7e) due to dissolution of ZnO NWs in the electrolyte and exposing Si NWs to the electrolyte, which will be discussed in the following section. Note that the stability test for this sample was performed after several different PEC tests; thus, the current degradation for a fresh bare b-NW sample is less than that observed for this sample. Also, note that for the J – V measurements of unprotected samples, measurements for several different current scans provided similar photocurrents (see Figure S7, Supporting Information), confirming that lack of long-term stability did not affect the J – V measurements. Furthermore, the consistent currents between the J – V and J – t measurements (Figure 4) as well as constant photocurrent during transient current density (Figure 4) further confirm that lack of long-term stability did not influence the J – V measurements. The TiO_2 -coated sample shows significant enhancement in the stability revealing that the complete coverage of TiO_2 layer on NWs well protects them. In general, the stability is bias or current dependence in which at higher biasing potentials or photocurrents, the stability reduces. Although the TiO_2/Pt -coated sample has much higher photocurrent than the TiO_2 -coated sample, it still shows dramatic enhancement in the stability. More importantly, we have shown stability of over 24 h under constant illumination for such a TiO_2/Pt -coated sample.²⁵ The time that the photocurrent needs to reach its plateau/saturation for TiO_2/Pt -coated sample is longer than that for TiO_2 -coated sample (Figure 7e), which may be due to slow Pt cocatalyst reaction though is not completely clear at this point.

The energy-dispersive X-ray spectroscopy (EDS) elemental mapping analyses for the bare and TiO_2/Pt coated b-NW samples for before and after stability tests are shown in Figure S8 (Supporting Information). The absence of Zn element in the elemental mapping of bare b-NW sample after the stability test shows the dissolution of ZnO NWs (Figure 7e), which can also clearly be seen in its SEM image (Figure S8b, Supporting Information). However, for the TiO_2/Pt -coated sample, all materials within the b-NWs remain after the stability test and ZnO NW branches do not dissolve in the electrolyte (see Figure S8d *versus* Figure S8c, Supporting Information, and their corresponding elemental mapping analyses), confirming that the TiO_2 coating layer well protects the NWs. In fact, shape and morphology of b-NWs remain unchanged after PEC measurements and long-term stability test (Figure S9, Supporting Information).

CONCLUSIONS

In summary, we report the systematic studies of 3D ZnO/Si b-NW photoelectrodes for solar water splitting and fuel generation. The PEC performance of the b-NW photoelectrodes with different sizes of NW cores/trunks and branches, different pitch sizes, and different doping concentrations of NW cores were tested in neutral medium. Larger ZnO NW branches and longer and denser p-Si NW cores gave higher photocathodic current, better efficiency, as well as lower photocurrent turn-on potential, while smaller ZnO NW branches and shorter p⁺-Si NW trunks offer higher photoanodic current and better efficiency. The optimized ZnO/p-Si b-NWs exhibited a significant photocathodic turn-on potential shift of ~ 600 mV compared to the bare p-Si NW array, as well as an energy conversion efficiency of $>2\%$ at -1 V *versus* Pt CE. Furthermore, by coating a thin TiO_2 protection layer using ALD, the stability of ZnO/Si b-NW photoelectrodes are remarkably improved. These results demonstrate that the b-NWs are effective photoelectrodes that offer enhanced photocurrent and photoresponse, reduced turn-on potential, increased conversion

efficiency, improved stability, and most importantly property tunability. These studies also provide useful insights in the design and fabrication of novel

3D b-NW electrodes based on cheap and earth abundant materials for potential high-efficiency and low-cost solar fuel generation.

METHODS

Fabrication of b-NW Electrodes. The device fabrication was carried out identically as reported previously.²⁵ Briefly, silicon substrates with different doping (p or p⁺) were patterned with an array of Ni disks using nanoimprint lithography and e-beam evaporation. RIE-ICP (reactive ion etching-inductively coupled plasma) dry etching was performed to fabricate vertical Si NW backbone arrays; NW lengths are determined by etching for various times with Ni disks as the etch mask. Followed by Ni removal and RCA cleaning,³⁰ the Si NW substrates were dried using N₂ and immediately transferred to the sputtering machine for the deposition of a thin ZnO layer, which later serves as seeding layer for ZnO NW growth. The measured thickness of sputtered ZnO on a glass slide was ~45 nm; however, its actual thickness on Si NW cores is smaller (for example, for 10m-Si NW cores, it was 25–30 nm). Finally, the ZnO NW branches were grown on the Si NW cores using a hydrothermal growth method.^{17,31} For the TiO₂-coated samples used for IPCE measurement and stability study, ALD was used to deposit 20 nm TiO₂ at a temperature of 250 °C. Three nm Pt cocatalyst was deposited on the TiO₂-coated b-NW substrates using e-beam evaporation.

Characterization. The samples morphologies were examined on a Philips XL30 field-emission environmental scanning electron microscope (ESEM) at an accelerating voltage of 10.0 kV. Energy-dispersive X-ray spectroscopy (EDS) and elemental mapping analyses were used to examine the material composition.

Photoelectrochemical and IPCE Measurements²⁵. Current density and IPCE measurements were performed in a 400 mL aqueous solution of 0.25 M Na₂SO₄ buffered at pH = 7.25 (neutral solution) with three electrodes configuration, including ZnO/Si b-NWs as working electrode (WE), Pt mesh as counter electrode (CE), and Ag/AgCl (1 M KCl) as reference electrode (RE). Light with a constant power intensity of 100 mW/cm² was adjusted at the samples position for the photocurrent measurements. A scan rate of 10 mV/s was used for the linear sweep voltammetry (LSV). During the J–V and IPCE measurements, a mild agitation was used and the electrolyte was constantly purged with a small flow of N₂ gas. All the external biasing potentials here are versus Ag/AgCl RE, unless otherwise stated.

Conflict of Interest: The authors declare no competing financial interest.

Acknowledgment. D.W. acknowledges the financial support for this work by the Department of Energy (DOE DE-FG36-08G018016) and the National Science Foundation (NSF ECCS0901113 and CBET1236155). D.W. also acknowledges the ONR-DURIP (N00014-08-1-0776) support for the ALD acquisition. D.W. thanks Drs. Ramesh Rao and Bernd Fruhberger for their unconditional support. A.K. acknowledges Sean Park, Xuekun Lu, and Ryan Anderson of UCSD NANO3 facilities for their unconditional and professional support. A.K. also acknowledges Salomon May for his drawing for the fabrication procedure. G.Y.J. was supported by the Basic Research Program through the National Research Foundation of Korea (NRF) funded by the Ministry of Science, ICT & Future Planning (No. R15-2008-006-03002-0, CLEA, NCRC).

Supporting Information Available: Efficiency calculation/plots, pitch size effect, elemental mapping analyses, and supporting images/plots. This material is available free of charge via the Internet at <http://pubs.acs.org>.

REFERENCES AND NOTES

- Wang, D.; Qian, F.; Yang, C.; Zhong, Z.; Lieber, C. M. Rational Growth of Branched and Hyperbranched Nanowire Structures. *Nano Lett.* **2004**, *4*, 871–874.

- Dick, K. A.; Deppert, K.; Larsson, M. W.; Martensson, T.; Seifert, W.; Wallenberg, L. R.; Samuelson, L. Synthesis of Branched “Nanotrees” by Controlled Seeding of Multiple Branching Events. *Nat. Mater.* **2004**, *3*, 380–384.
- Wang, D.; Lieber, C. M. Inorganic Materials: Nanocrystals Branch Out. *Nat. Mater.* **2003**, *2*, 355–356.
- Manna, L.; Milliron, D. J.; Meisel, A.; Scher, E. C.; Alivisatos, A. P. Controlled Growth of Tetrapod-Branched Inorganic Nanocrystals. *Nat. Mater.* **2003**, *2*, 382–385.
- Jiang, X.; Tian, B.; Xiang, J.; Qian, F.; Zheng, G.; Wang, H.; Mai, L.; Lieber, C. M. Rational Growth of Branched Nanowire Heterostructures with Synthetically Encoded Properties and Function. *Proc. Natl. Acad. Sci. U.S.A.* **2011**, *108*, 12212–12216.
- Cheng, H.-M.; Chiu, W.-H.; Lee, C.-H.; Tsai, S.-Y.; Hsieh, W.-F. Formation of Branched ZnO Nanowires from Solvothermal Method and Dye-Sensitized Solar Cells Applications. *J. Phys. Chem. C* **2008**, *112*, 16359–16364.
- Cho, I. S.; Chen, Z.; Forman, A. J.; Kim, D. R.; Rao, P. M.; Jaramillo, T. F.; Zheng, X. Branched TiO₂ Nanorods for Photoelectrochemical Hydrogen Production. *Nano Lett.* **2011**, *11*, 4978–4984.
- Jung, S.; Yong, K. Fabrication of CuO–ZnO Nanowires on a Stainless Steel Mesh for Highly Efficient Photocatalytic Applications. *Chem. Commun.* **2011**, *47*, 2643–2645.
- McCune, M.; Zhang, W.; Deng, Y. High Efficiency Dye-Sensitized Solar Cells Based on Three-Dimensional Multilayered ZnO Nanowire Arrays with “Caterpillar-like” Structure. *Nano Lett.* **2012**, *12*, 3656–3662.
- Qiu, Y.; Yan, K.; Deng, H.; Yang, S. Secondary Branching and Nitrogen Doping of ZnO Nanotetrapods: Building a Highly Active Network for Photoelectrochemical Water Splitting. *Nano Lett.* **2011**, *12*, 407–413.
- Sun, K.; Jing, Y.; Li, C.; Zhang, X.; Aguinaldo, R.; Kargar, A.; Madsen, K.; Banu, K.; Zhou, Y.; Bando, Y.; et al. 3D Branched Nanowire Heterojunction Photoelectrodes for High-Efficiency Solar Water Splitting and H₂ Generation. *Nanoscale* **2012**, *4*, 1515–1521.
- Xu, F.; Dai, M.; Lu, Y.; Sun, L. Hierarchical ZnO Nanowire–Nanosheet Architectures for High Power Conversion Efficiency in Dye-Sensitized Solar Cells. *J. Phys. Chem. C* **2010**, *114*, 2776–2782.
- Ahmad, M.; Yingying, S.; Nisar, A.; Sun, H.; Shen, W.; Wei, M.; Zhu, J. Synthesis of Hierarchical Flower-Like ZnO Nanostructures and Their Functionalization by Au Nanoparticles for Improved Photocatalytic and High Performance Li-ion Battery Anodes. *J. Mater. Chem.* **2011**, *21*, 7723–7729.
- Bierman, M. J.; Jin, S. Potential Applications of Hierarchical Branching Nanowires in Solar Energy Conversion. *Energy Environ. Sci.* **2009**, *2*, 1050–1059.
- Herman, I.; Yeo, J.; Hong, S.; Lee, D.; Nam, K. H.; Choi, J.-h.; Hong, W.-h.; Lee, D.; Grigoropoulos, C. P.; Ko, S. H. Hierarchical Weeping Willow Nano-Tree Growth and Effect of Branching on Dye-Sensitized Solar Cell Efficiency. *Nanotechnology* **2012**, *23*, 194005.
- Chen, W.; Qiu, Y.; Yang, S. Branched ZnO Nanostructures as Building Blocks of Photoelectrodes for Efficient Solar Energy Conversion. *Phys. Chem. Chem. Phys.* **2012**, *14*, 10872–10881.
- Sun, K.; Jing, Y.; Park, N.; Li, C.; Bando, Y.; Wang, D. Solution Synthesis of Large-Scale, High-Sensitivity ZnO/Si Hierarchical Nanoheterostructure Photodetectors. *J. Am. Chem. Soc.* **2010**, *132*, 15465–15467.
- Ko, S. H.; Lee, D.; Kang, H. W.; Nam, K. H.; Yeo, J. Y.; Hong, S. J.; Grigoropoulos, C. P.; Sung, H. J. Nanoforest of Hydrothermally Grown Hierarchical ZnO Nanowires for a High

- Efficiency Dye-Sensitized Solar Cell. *Nano Lett.* **2011**, *11*, 666–671.
19. Shao, F.; Sun, J.; Gao, L.; Yang, S.; Luo, J. Forest-Like TiO₂ Hierarchical Structures for Efficient Dye-Sensitized Solar Cells. *J. Mater. Chem.* **2012**, *22*, 6824–6830.
 20. Cheng, C.; Fan, H. J. Branched Nanowires: Synthesis and Energy Applications. *Nano Today* **2012**, *7*, 327–343.
 21. Li, C. C.; Yin, X. M.; Chen, L. B.; Li, Q. H.; Wang, T. H. High Capacity and Excellent Cycling Stability of Branched Cobalt Oxide Nanowires as Li-insertion Materials. *Appl. Phys. Lett.* **2010**, *97*, 043501.
 22. Zhou, W.; Cheng, C.; Liu, J.; Tay, Y. Y.; Jiang, J.; Jia, X.; Zhang, J.; Gong, H.; Hng, H. H.; Yu, T.; et al. Epitaxial Growth of Branched α -Fe₂O₃/SnO₂ Nano-Heterostructures with Improved Lithium-Ion Battery Performance. *Adv. Funct. Mater.* **2011**, *21*, 2439–2445.
 23. Liu, J.; Cheng, C.; Zhou, W.; Li, H.; Fan, H. J. Ultrathin Nickel Hydroxidenitrate Nanoflakes Branched on Nanowire Arrays for High-Rate Pseudocapacitive Energy Storage. *Chem. Commun.* **2011**, *47*, 3436–3438.
 24. Song, H. S.; Zhang, W. J.; Cheng, C.; Tang, Y. B.; Luo, L. B.; Chen, X.; Luan, C. Y.; Meng, X. M.; Zapfen, J. A.; Wang, N.; et al. Controllable Fabrication of Three-Dimensional Radial ZnO Nanowire/Silicon Microrod Hybrid Architectures. *Cryst. Growth Des.* **2010**, *11*, 147–153.
 25. Kargar, A.; Sun, K.; Jing, Y.; Choi, C.; Jeong, H.; Zhou, Y.; Madsen, K.; Naughton, P.; Jin, S.; Jung, G. Y.; et al. Tailoring n-ZnO/p-Si Branched Nanowire Heterostructures for Selective Photoelectrochemical Water Oxidation or Reduction. *Nano Lett.* **2013**, *13*, 3017–3022.
 26. Gray, H. B. Powering the Planet with Solar Fuel. *Nat. Chem.* **2009**, *1*, 7–7.
 27. Hou, Y.; Abrams, B. L.; Vesborg, P. C. K.; Björketun, M. E.; Herbst, K.; Bech, L.; Setti, A. M.; Damsgaard, C. D.; Pedersen, T.; Hansen, O.; et al. Bioinspired Molecular Co-Catalysts Bonded to a Silicon Photocathode for Solar Hydrogen Evolution. *Nat. Mater.* **2011**, *10*, 434–438.
 28. Henry, M. D. ICP Etching of Silicon for Micro and Nanoscale Devices. Ph.D. thesis, California Institute of Technology, 2010.
 29. Garnett, E.; Yang, P. Light Trapping in Silicon Nanowire Solar Cells. *Nano Lett.* **2010**, *10*, 1082–1087.
 30. Kern, W. The Evolution of Silicon Wafer Cleaning Technology. *J. Electrochem. Soc.* **1990**, *137*, 1887–1892.
 31. Law, M.; Greene, L. E.; Johnson, J. C.; Saykally, R.; Yang, P. Nanowire Dye-Sensitized Solar Cells. *Nat. Mater.* **2005**, *4*, 455–459.